PCCP

ROYAL SOCIETY OF CHEMISTRY

PAPER

View Article Online
View Journal | View Issue

Cite this: *Phys. Chem. Chem. Phys.*, 2025, **27**, 17376

First-principles investigation of nitrogen doping effects on the capacitance behavior of V_2CT_x MXenes†

Sruthi T., ‡*[a] Mandira Das‡[b] and Vincent Mathew[a]

Received 6th May 2025,
Accepted 21st July 2025

DOI: 10.1039/d5cp01703c

rsc.li/pccp

Hetero-atom doping is a widely employed strategy to enhance the desired properties of nanomaterials. In this study, we used density functional theory (DFT) to examine the impact of nitrogen doping on the electrochemical performance of V_2CT_x. By considering nitrogen incorporation at various sites, we found that lattice-site doping enhances charge storage capacity, whereas functional-site doping has the opposite effect. This enhancement arises from an increase in redox capacitance or pseudocapacitance, with surface redox activity being the primary mechanism driving the improved capacitance. We also explain the underlying reasons for the contrasting effects of these two doping sites on the electrochemical behavior of V_2CT_x.

1. Introduction

Electrochemical energy storage (EES) devices are pivotal in meeting the world's escalating energy demands while mitigating fossil fuel depletion. Among these, electrochemical capacitors (ECs), or supercapacitors, and secondary ion batteries stand out as transformative technologies. A supercapacitor comprises two electrodes separated by an electrolyte, storing energy through electrostatic double-layer capacitance (C_{EDL}) and redox capacitance (C_{redox}). The charge storage efficiency is governed by the electrode and electrolyte properties, with ideal electrodes exhibiting high surface area, superior electrical conductivity, thermal and chemical stability, and redox-active sites. The total capacitance (C_T) arises from C_{EDL}, C_{redox}, and an intrinsic electrode property known as quantum capacitance[1–3] (C_Q).

Carbon-based materials like activated carbon,[4,5] carbon nanotubes,[6,7] and carbon aerogels[8] were among the earliest electrode materials for ECs. Later, metal oxides (MnO_2,[9] RuO_2,[10] NiO,[11] *etc.*) emerged, offering redox-active sites that enhance redox capacitance and, consequently, total electrical capacitance (C_E). The discovery of graphene in 2004 revolutionized charge storage devices, as its high surface area, electrical conductivity, and tensile strength positioned it at the forefront of energy storage research.[12,13] Other two-dimensional materials, including transition metal dichalcogenides[14,15] (TMDs), h-boron nitride[16] (h-BN), silicene, and phosphorene,[17] have also shown potential as supercapacitor electrodes. In 2011, the introduction of MXenes, starting with $Ti_3C_2T_x$,[18] further advanced the field by combining a high surface area with surface redox activity, significantly enhancing electrochemical performance. MXenes are quasi-2D materials comprising multiple atomic layers, defined by the general formula $M_{n+1}X_n$, where M represents a transition metal, X denotes carbon or nitrogen, and n indicates the number of X layers. During chemical etching of the bulk MAX phase, surface functionalization occurs with groups such as –F, –O, and –OH, yielding functionalized MXenes[18] ($M_{n+1}X_nT_x$), where T represents the functional groups and x their relative proportion. $Ti_3C_2T_x$ exhibits substantially higher capacitance than graphene-based electrodes, with several other MXenes also demonstrating remarkable electrochemical performances.

Heteroatom doping and atomic substitution are well-established strategies for tailoring material properties. In various 2D materials – including graphene,[19] germanene,[20] phosphorene,[21] borophene,[22] and h-BN[23,24] doping with elements like nitrogen, oxygen, phosphorus, sulfur, and transition metals has significantly enhanced charge storage capacity. For $Ti_3C_2T_x$, nitrogen doping at low concentrations can boost storage capacity by an impressive 460%.[25] Both experimental and theoretical studies reveal that the electrochemical performance of nitrogen-doped $Ti_3C_2T_x$ is highly dependent on dopant site distribution, which directly influences C_{EDL} and C_{redox}.[25,26]

Since its discovery, $Ti_3C_2T_x$ has been extensively studied as an electrode material for supercapacitors and batteries. Another prominent member of the MXene family, vanadium-based V_2CT_x, has demonstrated outstanding electrochemical

[a] *Computational Nanoscience Lab, Department of Physics, Central University of Kerala, Kasaragod - 671320, India. E-mail: drsruthi2023@gmail.com*
[b] *Mechanical and Materials Engineering Department, University of Turku, 20100, Finland*

† Electronic supplementary information (ESI) available. See DOI: https://doi.org/10.1039/d5cp01703c

‡ These authors contributed equally.

performance. In an H_2SO_4 electrolyte, 2D V_2CT_x flakes exhibit a remarkable specific capacitance of 420 F g^{-1},[27] while Li, Na, and K intercalation yields capacitances ranging from 100 to 180 F g^{-1}. The fabricated electrode retains its full capacitance at 10 A g^{-1} and maintains 77% at 100 A g^{-1}, highlighting its robust rate capability. Additionally, spherical V_2CT_x achieves an impressive capacitance of 409 mAh g^{-1} in Zn-ion batteries at 0.5 A g^{-1}. V_2CT_x has also been incorporated into heterostructures with VS_2[28] and $Ti_3C_2T_x$,[29] further enhancing its electrochemical properties. Recent experimental findings indicate that nitrogen doping can amplify its capacitance threefold while maintaining excellent rate performance and cyclic stability for Zn ion batteries.[30] Another experiment and theoretical study explored the effect of nitrogen doping in V_2CT_x for supercapacitor applications.[31] However, a comprehensive understanding of how doping influences electrostatic double-layer (EDL) and redox capacitance remains limited.

In this study, we employ density functional theory (DFT) to investigate the effects of nitrogen doping on the electrochemical behavior of V_2CT_x. To model realistic surface chemistry, we consider varying –O and OH functionalization as –F functionalization is not redox active, representing its evolution from V_2CO_2 to $V_2C(OH)_2$. Furthermore, we systematically analyze how dopant site distribution modulates EDL, redox, and quantum capacitance considering a doping concentration of 10%. This in-depth theoretical exploration aims to provide experimentalists with valuable insights into optimizing electrochemical performance through strategic doping.

2. Methodology

2.1. Modeling of the doping-functionalized MXenes

V_2C is modeled by removing the 'Al' layer from the bulk MAX phase V_2AlC structure. The monolayer V_2C is a three-atomic layer thick material, where the 'C' layer is sandwiched between two 'V' layers as shown in Fig. 1(b) [side view]. In order to model O-functional V_2C, we consider three possible sites at the MXene surface for –O atoms to become attached. Fig. 1(a) and (b) show the top and side view of the V_2C MXene, marking the possible functional site. The descriptions of the sites are as following: (a) site T: top of the 'V' atoms, (b) site H: hollow site of the 'V' atom of further surfaces and (c) site C: hollow site of the 'C' atoms. Three sites and two equivalent surfaces result in six possible functionalized structures. The atomistic simulation reveals that

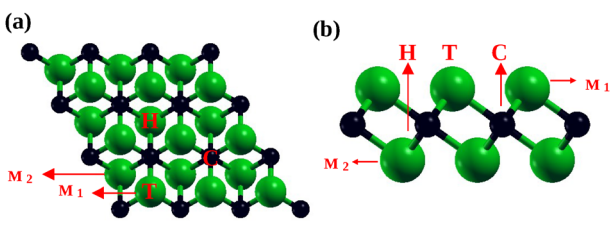

Fig. 1 (a) Top and (b) side view of V_2C. The available sites for functional elements are 'H', 'T' and 'C'. Green and black balls represent the 'V' and 'C' atoms respectively.

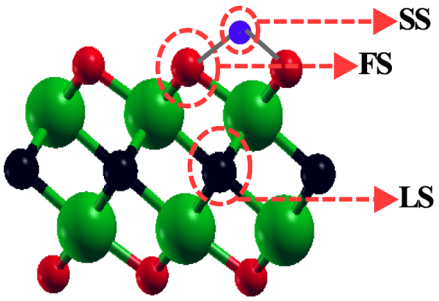

Fig. 2 Different doping sites, lattice-site (LS), functional-site (FS) and surface-site (SS), are presented.

site 'H' is energetically stable on both of the V_2C surfaces. The energetically stable O-functional V_2C structure is shown in Fig. 2 and represented as V_2CO_2. Our finding is consistent with the reported literature.[32]

We started with V_2CO_2 to model the nitrogen doping. While doping the MXene with the 'N' atom, one must consider the size and mass of it. Nitrogen can either replace the carbon atoms or the oxygen atoms due to comparable mass and size. Another possibility is it will sit on the MXene surface without replacing any elements. We assigned the names 'lattice-site' (LS) and 'functional-site' (FS) for when carbon and oxygen were replaced, respectively, as shown in Fig. 2. While nitrogen sits on the surface of the MXene, we marked it as the 'surface-site' (SS) (Fig. 2). The formation energy of the doped MXene is computed using eqn (1).

$$E_{\text{form}} = E_{\text{doped}} - \left(E_{\text{undoped}} + n \times \left(\frac{E_{N_2}}{2}\right)\right) \quad (1)$$

where E_{doped} and E_{undoped} are the energies of the doped and undoped systems, respectively. n is the number of doped nitrogen atoms, and E_{N_2} is the energy of the nitrogen molecule.

The total energies and electronic structure are calculated using the DFT-based projector augmented wave method,[33,34] as implemented in Vienna *ab initio* Simulation Package (VASP).[33,34] The exchange–correlation part of the Hamiltonian is described by the Perdew–Burke–Ernzerhof (PBE) generalized gradient approximation (GGA).[35] We investigated the stable structure of O-functional MXenes using the unit cell of V_2C. We used a kinetic energy cut-off of 520 eV and a Monkhorst–pack[36] (MP) grid of $12 \times 12 \times 1$ for self-consistent calculation. A finer k-mesh of $24 \times 24 \times 1$ is used to compute the electronic structure of the systems. We chose the $3 \times 3 \times 1$ supercell to model the N-doped MXenes as this size is enough to maintain the doping concentration at 10%. A kinetic energy cut-off of 520 eV and MP grid of $6 \times 6 \times 1$ were used for self-consistent calculation of the doped MXenes. A finer k-mesh of $12 \times 12 \times 1$ is used to compute the densities of states of the doped systems. The convergence criteria for energy and force were set to 10^{-6} eV and 0.05 eV $Å^{-1}$, respectively.

2.2 Calculation of quantum capacitance (C_Q)

The total capacitance (C_T) of a supercapacitor is the series combination of electrical capacitance (C_E) and quantum

capacitance (C_Q) and given by eqn (2)

$$\frac{1}{C_T} = \frac{1}{C_E} + \frac{1}{C_Q} \quad (2)$$

Electrochemical double layer capacitance (C_{EDL}) and redox capacitance (C_{redox}) combines in parallel to give total electrical capacitance (C_E), given by eqn (3)

$$C_E = C_{EDL} + C_{redox} \quad (3)$$

Quantum capacitance arises due to the intrinsic property of the electrode.[1,37,38] The change in the electronic states near the Fermi level on application of electrode potential during operation results in the quantum capacitance. Quantum capacitance is much higher than the electrical capacitance for a three-dimensional electrode material and results in negligible contribution to the total capacitance according to eqn (2). However, in the case of the two-dimensional electrode, the C_Q is of close order to C_E thus cannot be neglected while computing total capacitance (C_T).

The differential quantum capacitance (C_Q^{diff}) is related to the densities of states of the electrode material around the Fermi level by the following equation,

$$C_Q^{diff} = \frac{e^2}{4k_B T}\int_{-\infty}^{+\infty} D(\varepsilon)\mathrm{sech}^2\left(\frac{\varepsilon - eV}{k_B T}\right)d\varepsilon \quad (4)$$

where $D(\varepsilon)$ is the densities of states of the electrode material. We set the temperature value at 300 K, the room temperature. The whole picture of quantum capacitance is given by integrating the C_Q^{diff} in the voltage range of 0 to v Volt, given by eqn (5),

$$C_Q^{int} = \frac{1}{ev}\int_0^v C_Q^{diff} dV \quad (5)$$

C_Q^{int} is the variation of quantum capacitance (C_Q) in the operating voltage range.

2.3. Modeling the electrode–electrolyte interaction and computation of the capacitance

As discussed earlier, the contribution to the electric capacitance, C_E is 2-fold: one due to the formation of electronic double layer of ions on the electrode that gives rise to C_{EDL} and the other is charge transfer across the double layer between the ions and the electrode and gives rise to C_{redox}. We applied a formalism[39] by Wang *et al*. to compute the redox capacitance. This formalism considers two assumptions: (a) the electrode is negatively charged and (b) the electrolyte contains H^+ as the positive ion. The H^+ ions get physically adsorbed on the electrode surface during the charging process. We are modeling that situation by adsorbing H on the 3 × 3 × 1 cell of the electrode one by one till we reach the full H-coverage. The systematic adsorption of H on the electrode will not change the electronic structure of the electrode, rather will shift the densities-of-states. This in known as 'Rigid band approximation (RBA)'. The redox capacitance (C_{redox}) is given by eqn (6).

$$C_{redox} = \frac{\Delta Q}{\Delta V} \quad (6)$$

where ΔQ is the charge transfer between the H^+ ion and the charged electrode and ΔV is the change in voltage due to the transfer. ΔV is related to the change in the work-function (ΔWF) by eqn (7) and ΔWF is given by eqn (8).

$$\Delta V = \Delta WF/e \quad (7)$$

$$\Delta WF = WF - (WF^{neutral} - \Delta E_f) \quad (8)$$

where WF and WF^{neutal} are the work-function of the electrode H ion adsorption and neutral electrode, respectively. ΔE_f is the amount of the Fermi shift due to H adsorption. The work function of the electrode is calculated using the energy of vacuum (E_{vac}) and Fermi level (E_f) by eqn (9).

$$WF = E_{vac} - E_f \quad (9)$$

C_{EDL} is calculated by the usual formula,

$$C_{EDL} = \frac{\varepsilon_0 \varepsilon_r A}{d} \quad (10)$$

where, ε_0, ε_0, A and d are the permittivity of the free space, dielectric constant of the electrolyte, surface area of the electrode and the width of the double layer at the electrode, respectively.

3. Results and discussions

3.1. Structural stability

As discussed in Section 2.1, we constructed three models of N-doped V_2CO_2 MXenes and calculated their formation energy using eqn (1). The 'SS' model was found to be unstable, as its structure collapsed during the self-consistent calculation. In contrast, the 'LS' and 'FS' models exhibited energetic stability, as indicated by their negative formation energy (E_{form}) in Table 1.

A closer examination of Table 1 reveals that the lattice site ('LS') is energetically more favorable than the functional site ('FS') for nitrogen incorporation at both doping concentrations. Furthermore, the formation energy increases with doping concentration, suggesting that the 10% doped model is more stable than the 11% doped one. The final optimized side and top view structures of the 'LS' and 'FS' doped V_2CO_2 configurations are depicted in Fig. 3.

3.2. Electronic structure and quantum capacitance

As discussed in Section 2.2, quantum capacitance depends on the electronic structure of the system near the Fermi level. Fig. 4(a) presents the total and partial densities of states (DOS)

Table 1 Formation energy (E_{form}) in eV of doped MXenes (LS and FS) for different doping concentrations

System	Doping concentration (%)	E_{form} (eV per atom)
LS	10	−7.18
	11	−5.21
FS	10	−6.72
	11	−4.66

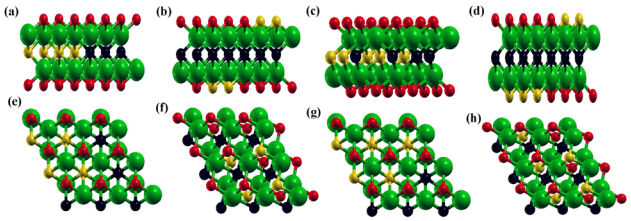

Fig. 3 Optimized ground-state structures of N-doped V_2CO_2: side views of (a) LS (10%), (b) FS (10%), (c) LS (11%), and (d) FS (11%); (e)–(h) show the corresponding top views of structures (a)–(d). Red, green, yellow, and black spheres represent O, V, N, and C atoms, respectively.

of the constituent elements of V_2CO_2 within the energy range of −2.0 to +1.5 eV, with the Fermi level set at 0 eV. The contributions from carbon and oxygen are highlighted in the inset of Fig. 4(a). The d-electron states of vanadium predominantly contribute to the total electronic structure around the Fermi level, while the p-electrons of carbon and oxygen contribute at deeper energy levels (not shown in Fig. 4(a)).

Fig. 4(b) illustrates the variation of integrated quantum capacitance (C_Q^{int}) as a function of applied electrode voltage, ranging from ±1 V, for pristine V_2CO_2 in units of F g^{-1}. This voltage range is selected based on the electrochemical stability window of 1.25 V for an acidic aqueous electrolyte at room temperature. The variation of C_Q^{int} within the ±1 V range closely reflects the electronic structure near the Fermi level. C_Q^{int} attains its minimum value around 0 V and increases with voltage in both directions. However, it reaches its highest value around +0.7 V. The lower number of available states in the occupied region leads to a smaller C_Q^{int} in the negative voltage range compared to the positive region, where it reaches a maximum at approximately −0.5 V.

Fig. 5(a) and (b) illustrate the electronic structure of doped V_2CO_2, where nitrogen replaces carbon atoms at the lattice site (LS) for concentrations of 10% and 11%. Nitrogen has one more valence electron than carbon and one less than oxygen. When nitrogen substitutes carbon, the total number of electrons in the system increases, causing a shift in the density of states towards lower energy levels. In pristine MXenes (Fig. 4(a)), a density peak appears at 0.2 eV in the unoccupied region, which shifts to 0 eV (Fig. 5(a)) and further to −0.2 eV (Fig. 5(b)) after carbon is replaced by nitrogen at the lattice site. The contribution of nitrogen to the overall electronic structure is highlighted in the corresponding inset figures. This shift in the density peak near the Fermi level influences C_Q^{int}, as shown in Fig. 5(c). The integrated quantum capacitance exhibits a similar trend in the positive voltage region to that of the pristine system for both doping concentrations. However, a dip in the electronic structure around the Fermi level in LS-doped V_2CO_2 leads to the lowest C_Q^{int} value near 0 V for both cases. Additionally, in the negative voltage region, C_Q^{int} decreases compared to the pristine material. Fig. 5(d) and (e) depict the electronic structure of V_2CO_2 when nitrogen occupies the functional site (FS), replacing oxygen atoms. In FS-doped V_2CO_2, the total number of electrons decreases, causing a shift in the electronic structure towards higher energy states, as observed in Fig. 5(d) and (e). The peak at −0.5 eV in the occupied region of pristine V_2CO_2 shifts closer to the Fermi level with reduced intensity in FS-doped MXenes (see Fig. 4(a) and 5(d) and (e)). This shift in the electronic structure affects the variation of C_Q^{int} with electrode potential. Fig. 5(f) illustrates the C_Q^{int} dependence on electrode potential for FS-doped V_2CO_2. In the positive voltage region, the highest C_Q^{int} value decreases by 400 F g^{-1} for FS-doped MXenes compared to both pristine and LS-doped MXenes. However, in the negative voltage region, C_Q^{int} increases

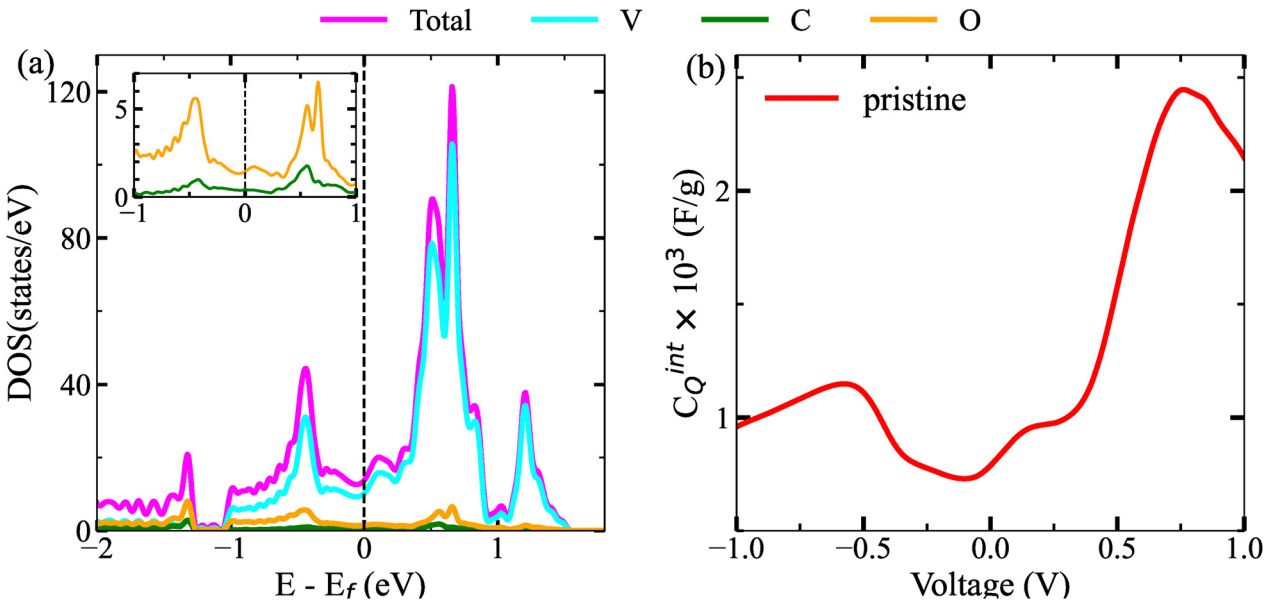

Fig. 4 (a) Electronic structure of pristine V_2CO_2. Total and partial densities of states of vanadium, carbon (inset) and oxygen (inset) are shown. Magnified version of C and O contributions are presented in the inset. (b) Variation of C_Q^{int} with units of F g^{-1} with applied electrode voltage for pristine MXenes.

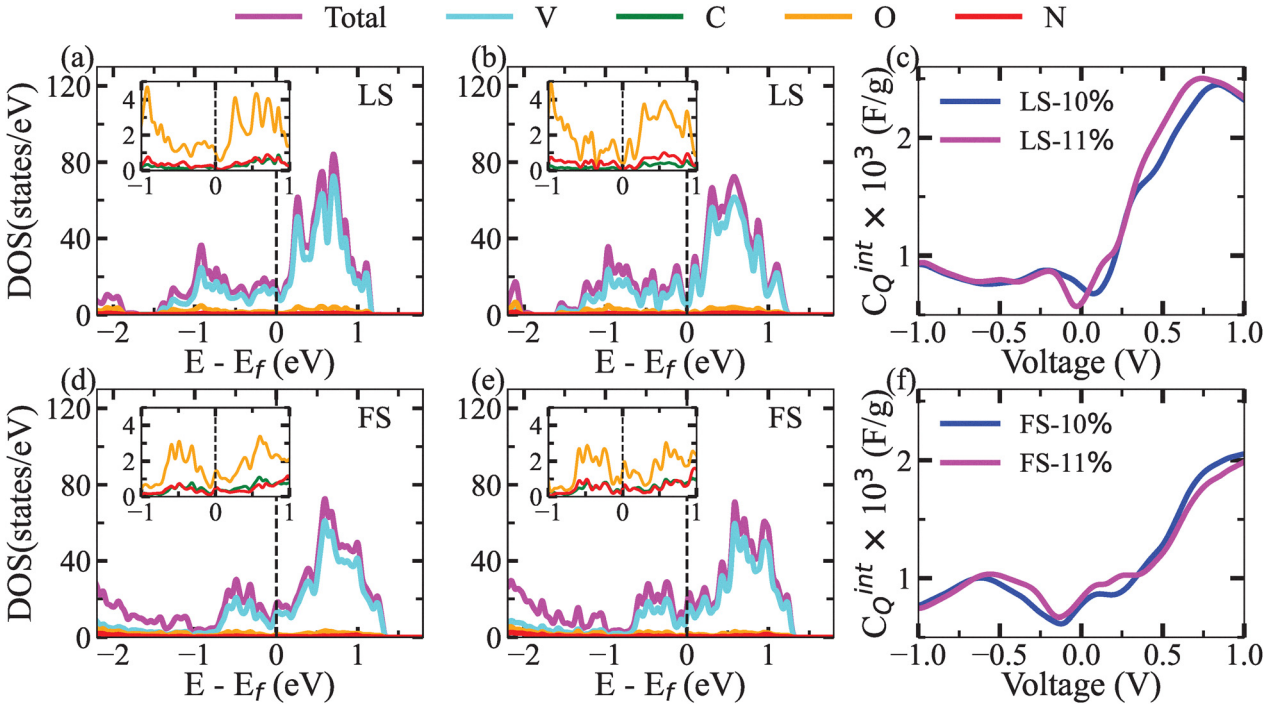

Fig. 5 (a) and (b) Electronic structure for 10% and 11%, and (c) C_Q^{int} *vs.* voltage of LS doped V_2CT_x. (d) and (e) electronic structure for 10% and 11%, and (f) C_Q^{int} *vs.* voltage of FS doped V_2CT_x.

for FS-doped MXenes relative to LS-doped MXenes, with a peak appearing around −0.6 V (Fig. 5(c)).

A close examination of C_Q^{int} behavior after doping at different sites reveals the following: (a) functional-site doping has a significant impact on integrated quantum capacitance, (b) in the positive voltage region, only vanadium d-electrons contribute to the C_Q^{int} value across all systems. Throughout the chosen electrode potential window, the integrated quantum capacitance fluctuates during the experiment. Additionally, the total capacitance (C_T) varies in accordance with C_Q^{int}, as described by eqn (2). The next subsection explores the electrochemical performance of the selected MXene electrodes.

Table 2 C_{redox} and C_{EDL} of pristine and doped MXenes for different concentrations. Average charge transfer (ΔQ) (*e*), change in work-function (ΔWF), Fermi-shift (ΔE_f), and work-function of neutral ($WF^{neutral}$) and full H (WF) covered electrodes

System	Doping %	C_{redox} (F g^{-1})	C_{EDL} (F g^{-1})	Avg ΔQ (*e*)	ΔWF (eV)	ΔE_f (eV)	WF (eV)	$WF^{neutral}$ (eV)
Pristine	—	162.04	56.21	0.480	3.90	0.52	2.20	6.62
LS	10	167.94	55.29	0.472	3.64	0.48	2.17	6.29
	11	188.64	55.21	0.477	3.27	0.48	2.48	6.23
FS	10	144.92	55.96	0.492	4.45	0.45	1.56	6.46
	11	147.84	56.04	0.499	4.43	0.45	1.60	6.48

3.3 Electrochemical performance

The redox, or pseudo-capacitance, arises from the faradaic charge transfer between the adsorbed hydrogen ion and the charged electrode. We utilize eqn (6)–(9) to calculate C_{redox}, as elaborated in Section 2.3. The electrochemical double-layer capacitance (C_{EDL}) is determined using eqn (10), which is solely dependent on the electrode's surface area, while other parameters (ε_0, ε_r, and d) remain invariant for a given electrolyte. Table 2 reports the values of C_{redox} and C_{EDL} for both pristine and doped MXene, expressed in F g^{-1}. The EDL capacitance decreases by 0.3–0.44% for FS-doped MXene and by 1.63–1.77% for LS-doped MXene as the doping concentration increases from 10% to 11%. This decline in C_{EDL} is primarily attributed to alterations in the lattice parameters and the electrode's mass.

In general, the C_{redox} of both pristine and doped systems is approximately three times greater than C_{EDL}, as illustrated in Table 2. When nitrogen doping occurs at carbon sites, C_{redox} exhibits an increase of 3.64% and 16.41% for doping concentrations of 10% and 11%, respectively. However, this trend reverses when nitrogen substitutes oxygen at the functional site, resulting in a decline of 10.56% and 8.76% in C_{redox} for 10% and 11% doping concentrations, respectively. To elucidate the underlying factors influencing redox capacitance, we present the key contributing parameters to C_{redox} in Table 2. These parameters encompass the average charge transfer (ΔQ), change in work function (ΔWF), Fermi level shift (ΔE_f), and the work function of the neutral electrode ($WF^{neutral}$) and full H covered electrode (WF).

Before delving into the detailed analysis of ΔQ and ΔWF for pristine and doped MXenes, it is essential to first examine the trend in the work function for pristine and doped MXenes under neutral conditions ($WF^{neutral}$). The following analysis

provides insights into these variations. (a) In the LS-doped system, $WF^{neutral}$ decreases by 5% and 5.89% compared to the pristine system. In the case of carbon-to-nitrogen substitution in V_2CO_2, Bader analysis shows that the vanadium atom bonded to nitrogen has a lower charge ($\sim$10.98 e) compared to the pristine one ($\sim$11.23 e), indicating it donates more electrons upon doping. Nitrogen, being more electronegative than carbon, attracts more charge, increasing electron localization around itself. This charge re-distribution creates a stronger local dipole pointing inward (from vanadium to inner layer), which can lower the electrostatic potential inside the slab and thus pull the Fermi level downward. However, because the nitrogen layer is still subsurface (unlike FS doped MXenes), the overall surface dipole weakens, leading to a reduced vacuum level. The net effect is a decrease in the work function, driven by a combined shift of both the Fermi level (downward) and the vacuum level (even more downward). (b) For the FS-doped system, it decreases by 2.71% and 2.11% compared to the pristine system. Upon replacing oxygen with nitrogen, Bader charge analysis shows that vanadium atoms retain slightly more electrons (increasing from $\sim$11.23 e to 11.33 e), meaning they donate less charge upon doping. This is because nitrogen is less electronegative than oxygen, and thus draws fewer electrons toward the surface. As a result, more electron density remains localized near the vanadium layer, increasing the overall electron concentration in the slab. This leads to an upward shift in the Fermi level, as the electronic states are more filled. Meanwhile, the surface dipole weakens due to reduced charge transfer toward the surface, which lowers the vacuum level slightly. The combined effect of higher Fermi level and slightly lower vacuum level results in a decrease in the work function.

For an electrode with full H-coverage, we observed the following for pristine and doped MXenes:

1. $\Delta E_f^{pristine} > \Delta E_f^{LS} > \Delta E_f^{FS}$, though the difference is the range of 0.04–0.07 eV for LS and FS doped systems.

2. $\Delta Q^{pristine} > \Delta Q^{LS}$ and $\Delta Q^{pristine} < \Delta Q^{FS}$ for both 10% and 11% doping concentrations. ΔQ always increases with doping concentrations, true for both doping sites.

3. $\Delta WF^{pristine} > \Delta WF^{LS}$ and $\Delta WF^{pristine} < \Delta WF^{FS}$ for both 10% and 11% concentrations. ΔWF always decreases with concentration, true for both doping sites.

4. $WF^{pristine} > WF^{FS}$, work-function increases with concentrations for the 'FS' system. However, this trend is quite dramatic for the 'LS' system, as it decreases for 10% concentration and with 11% doping it increases compared with the pristine one.

It is observed from the trends discussed above that the charge transfer (ΔQ) and change in work function (ΔWF) depend on both the doping sites and concentrations. Therefore, understanding the changes in the redox capacitance (C_{redox}) following doping requires considering both of these factors. In the case of LS-doped MXenes, the decrease in charge transfer (ΔQ) to the adsorbed hydrogen ion, compared to the pristine system, can be explained by the significant electronegativity difference between nitrogen and carbon, as well as the bond distances between V–N and V–C. Nitrogen has an electronegativity of 3.04, which is much higher than that of carbon (2.55), while the bond distances for V–N and V–C are 1.94 Å and 1.93 Å, respectively. Due to its higher electronegativity, nitrogen attracts greater electron density towards itself. When nitrogen replaces carbon, despite having a similar bond distance as carbon with the outer vanadium layer, nitrogen pulls electron density away from the surface, resulting in a lower electron density on the outer oxygen layer, which leads to less charge transfer to the hydrogen ion compared to the pristine system. A reverse trend is observed when nitrogen replaces oxygen at the functional site. Nitrogen, being less electronegative than oxygen (3.44), tends to donate more electron density to the adsorbed hydrogen ion. This explains the higher ΔQ for the FS-doped system compared to the pristine system. The ΔWF depends on three factors: (a) the work function of the electrode with full hydrogen coverage (WF), (b) the work function of the electrode with no hydrogen coverage ($WF^{neutral}$), and (c) the shift in the Fermi level (ΔE_f) due to hydrogen adsorption. Regardless of the doping sites, ΔE_f is not a dominant factor, as the change in it upon doping is not significant. The substantial change in work function before and after hydrogen adsorption reflects a shift in the surface dipole moment due to the formation of OH bonds on the surface. The next question is why there is such a significant change in WF when transitioning from pristine to LS and FS-doped systems, and the explanations for these contributions are as follows:

1. When V_2CT_x is doped with nitrogen at the lattice site with a 10% concentration, the $WF_{full\text{-}H}$ decreases by 0.03 eV compared to the pristine system. However, it increases by 0.28 eV when the doping concentration is increased by 1%. A possible explanation for this dramatic behavior of WF is that, at lower doping concentrations, the electronic states at the surface are not significantly perturbed, leading to only a small change. However, as more nitrogen is added to the system, the effect on the surface dipole and charge redistribution becomes more pronounced, resulting in a larger change in the work function.

2. In the case of FS-doped V_2CT_x, WF decreases significantly compared to the pristine system. The reason for this drastic change is the reduction in oxygen content on the MXene surface. The –OH bonds in the pristine system generate a strong surface dipole, while nitrogen atoms cannot form such strong bonds with the adsorbed hydrogen ions, leading to the disruption of the surface dipole. The slight increase in WF with a 1% increase in doping concentration is attributed to a change in electron density, but the overall trend remains a significant reduction compared to the pristine MXenes.

Having explained all the factors affecting the C_{redox}, the following is a quantitative analysis of the C_{redox} trend for the doped systems: (a) ΔQ decreases by 1.6% and 0.6%, while ΔWF decreases by 6.7% and 16.15% for LS-doped V_2CT_x. Since ΔWF inversely affects C_{redox}, the reduction in ΔWF increases the C_{redox} for LS-doped V_2CT_x compared to the pristine system, even though ΔQ decreases, (b) in the case of FS-doped V_2CT_x, ΔQ increases by 2.5% and 3.9%, and ΔWF increases by 14.1% and 13.6% for 10% and 11% doping, respectively. The substantial

Table 3 Electrical (C_E), integrated quantum capacitance (C_Q^{int}) and total capacitance (C_T) of the pristine and doped MXenes

System	Doping (%)	C_E (F g^{-1})	C_Q^{int} (F g^{-1})			C_T (F g^{-1})		
			0 V	−0.6 V	−1.0 V	0 V	−0.6 V	−1.0 V
Pristine	—	218.25	787.00	1147.22	956.73	170.87	183.37	177.71
LS	10	223.23	738.19	761.21	925.80	171.40	172.44	179.86
	11	243.85	595.23	783.05	933.71	172.98	185.94	193.35
FS	10	200.88	775.88	1000.90	765.74	159.58	167.30	159.13
	11	203.88	829.45	1027.57	742.75	163.65	170.13	159.96

increase in ΔWF leads to a significant decrease in C_{redox} for the FS-doped system compared to the pristine one. After examining the trends in C_{redox} and C_{EDL}, it is now time to explore the trend in total capacitance (C_T). The quantum capacitance (C_Q) plays a significant role in determining C_T for a two-dimensional electrode material. In the following section, we discuss the trend in C_T.

3.4. Total capacitance

Total electrical capacitance (C_E) and quantum capacitance (C_Q) together determine the total capacitance (C_T) as described in eqn (2). C_E, which reflects the electrochemical performance, is calculated using eqn (3). Table 3 presents the electrochemical capacitances (C_{EDL}, C_{redox}, and C_E), quantum capacitance (C_Q^{int}), and total capacitance (C_T) collectively. As discussed in Section 2.2, quantum capacitance plays a crucial role in defining the total charge storage capacity of two-dimensional materials. From Table 3, it is evident that C_Q^{int} is of the same order of magnitude as C_E and cannot be overlooked when determining C_T. According to eqn (2), the total capacitance (C_T) becomes lower than the smallest individual capacitance. To determine C_T, we selected three values of C_Q^{int} at voltages 0 V, −0.6 V, and −1.0 V. These extreme values were chosen for the following reasons: (a) C_Q^{int} varies with the applied voltage, (b) C_Q^{int} reaches a minimum around 0 V for both pristine and doped systems, (c) the electrode is assumed to be negatively charged, making −1 V the maximum applied voltage, and (d) except for the LS-doped system, other systems exhibit a maximum C_Q^{int} around −0.6 V.

One major limitation of our methodology for determining C_{EDL} and C_{redox} is that their variation with the applied voltage remains unknown. By selecting C_Q^{int} at three different values, we can provide the two extreme values (maximum and minimum) of C_T for both pristine and doped systems, with the total capacitance expected to vary between these extremes as the applied voltage changes. In pristine and FS-doped systems, C_Q^{int} reaches a maximum around −0.6 V and two minima at 0 V and −1 V, resulting in the highest C_T value around −0.6 V. However, in the LS-doped system, C_T reaches its maximum around −1 V, following the trend of C_Q^{int}.

A direct one-to-one correspondence between our results and experimental data is not feasible. Experimentally, storage capacity is determined from cyclic voltammograms (charge *vs.* voltage). The electrochemical performance of an electrode depends on several factors, including (a) the electrolyte used, (b) the synthesis process of the electrode, and (c) the voltage scan rate during the experiment. However, a rough comparison between our findings and available experimental results can still be made. We compare our results with an experiment that investigates the site-dependent nitrogen doping effect on the electrochemical performance of V_2CT_x in the presence of a 1 M H_2SO_4 electrolyte. That study reported a capacitance of 464.4 F g^{-1} for pristine V_2CT_x, which increased to 592.9 F g^{-1} when doped with nitrogen at a scan rate of 2 mV s^{-1}. Experimentally, the capacitance increased by 27%,[31] whereas our calculations show an increment ranging from 2.71% to 13.55% in total capacitance, depending on the applied voltage. The study attributed the enhancement to electronic structure and work function calculations, suggesting that functional-site doping enhances redox capacitance, while lattice-site doping increases EDL capacitance. However, our findings contradict this claim.

4. Conclusions

V_2CT_x is one of the most extensively studied MXenes for electrochemical electrode applications, second only to $Ti_3C_2T_x$. Numerous experiments have explored strategies such as doping, hetero-structure formation, and surface engineering to enhance the charge storage capacity of V_2CT_x. In this study, we employ first-principles calculations to investigate the effect of nitrogen doping at different sites on the electrochemical performance of V_2CT_x. Specifically, we analyze how doping influences charge transfer and work function variation – two key factors that determine redox capacitance. Additionally, we examine the role of quantum capacitance in the overall capacitance. Nitrogen doping was introduced at both lattice sites and functional sites at concentrations of 10% and 11%. Our findings indicate that lattice-site doping is more effective than functional-site doping in enhancing charge storage capacity. However, this result contradicts a previously reported study. Moreover, the increase in total capacitance observed in our calculations is significantly lower than that reported in experimental studies on nitrogen-doped V_2CT_x. A limitation of our methodology is that it does not capture the variation of C_{redox} and C_{EDL} with applied electrode potential. Future studies could extend this work using advanced methodologies that explicitly account for the effect of electrode potential on C_{redox}. This research provides a framework for investigating the impact of hetero-atom doping in nanomaterials for electrode applications.

Conflicts of interest

There are no conflicts to declare.

Data availability

The Vienna *Ab initio* Simulation Package (VASP) is used for electronic structure calculations and is available at **https://www.vasp.at**. The version employed in this study is VASP 5.4.4.

Acknowledgements

The first author gratefully acknowledges the Kerala State Council for Science, Technology, and Environment (KSCSTE), Kerala, India, for granting a post-doctoral fellowship that supported this research. The first author, Sruthi T., gratefully acknowledges the computational facilities provided by the Central University of Kerala.

References

1 S. Luryi, *Appl. Phys. Lett.*, 1988, **52**, 501–503.
2 T. Sruthi and K. Tarafder, *J. Phys.: Condens. Matter*, 2019, **31**, 475502.
3 T. Sruthi and K. Tarafder, *Bull. Mater. Sci.*, 2019, **42**, 257.
4 H. I. Becker, Low voltage electrolytic capacitor, *US Pat.*, 2800616, 1957.
5 A. Platek-Mielczarek, J. Conder, K. Fic and C. M. Ghimbeu, *J. Power Sources*, 2022, **542**, 231714.
6 L. F. Aval, M. Ghoranneviss and G. B. Pour, *Heliyon*, 2018, **4**, e00862.
7 S. Tan, J. Li, L. Zhou, P. Chen, J. Shi and Z. Xu, *Polymers*, 2018, **10**, 1072.
8 Y. J. Lee, G.-P. Kim, Y. Bang, J. Yi, J. G. Seo and I. K. Song, *Mater. Res. Bull.*, 2014, **50**, 240–245.
9 H. Begum, M. S. Ahmed, S. Cho and S. Jeon, *J. Power Sources*, 2017, **372**, 116–124.
10 J.-C. Chou, Y.-L. Chen, M.-H. Yang, Y.-Z. Chen, C.-C. Lai, H.-T. Chiu, C.-Y. Lee, Y.-L. Chueh and J.-Y. Gan, *J. Mater. Chem. A*, 2013, **1**, 8753–8758.
11 M. Yu, W. Wang, C. Li, T. Zhai, X. Lu and Y. Tong, *NPG Asia Mater.*, 2014, **6**, e129–e129.
12 Q. Ke and J. Wang, *J. Materiomics*, 2016, **2**, 37–54.
13 X. Yu, S. K. Park, S.-H. Yeon and H. S. Park, *J. Power Sources*, 2015, **283**, 328.
14 H. Lei, M. Wang, J. Tu and S. Jiao, *Sustainable Energy Fuels*, 2019, **3**, 2717–2724.
15 P. Sharma, A. Kumar, S. Bankuru, J. Chakraborty and S. Puravankara, *New J. Chem.*, 2020, **44**, 1594–1608.
16 D. Sun, Z. Sun, D. Yang, X. Jiang, J. Tang and X. Wang, *EcoEnergy*, 2023, **1**, 375–404.
17 S. Venkateshalu, G. Subashini, P. Bhardwaj, G. Jacob, R. Sellappan, V. Raghavan, S. Jain, S. Pandiaraj, V. Natarajan and B. A. M. Al Alwan, *et al.*, *J. Energy Storage*, 2022, **48**, 104027.
18 M. Naguib, M. Kurtoglu, V. Presser, J. Lu, J. Niu, M. Heon, L. Hultman, Y. Gogotsi and M. W. Barsoum, *MXenes*, Jenny Stanford Publishing, 2023, pp. 15–29.
19 Q. Zhou, W. Ju, Y. Yong, Q. Zhang, Y. Liu and J. Li, *Carbon*, 2020, **170**, 368–379.
20 X. Si, W. She, Q. Xu, G. Yang, Z. Li, S. Wang and J. Luan, *Materials*, 2021, **15**, 103.
21 A. Tiwari, G. Bansal, S. J. Mukhopadhyay, A. Bhattacharjee and S. Kanungo, *J. Energy Storage*, 2023, **73**, 109040.
22 J. Jalilian, G. Rezaei, B. Vaseghi, E. Zare, F. Taghizadeh and H. A. Mardani-Fard, *J. Energy Storage*, 2025, **107**, 114843.
23 T. Sruthi and V. Mathew, *IOP Conf. Ser.: Mater. Sci. Eng.*, 2024, 012001.
24 S. Thomas, S. Thulaseedasan and M. Asle Zaeem, *FlatChem*, 2022, **35**, 100414.
25 Y. Wen, T. E. Rufford, X. Chen, N. Li, M. Lyu, L. Dai and L. Wang, *Nano Energy*, 2017, **38**, 368–376.
26 M. Das and S. Ghosh, *J. Electrochem. Soc.*, 2022, **169**, 090525.
27 S. A. Zahra, M. M. Murshed, U. Naeem, T. M. Gesing and S. Rizwan, *Chem. Eng. J.*, 2023, **474**, 145526.
28 F. Yu, Z. Yang, X. Zhang, P. Yang, L. Li and J. Ma, *J. Mater. Chem. A*, 2022, **10**, 23531–23541.
29 K. Chen, Y. Guan, Y. Cong, H. Zhu, K. Li, J. Wu, Z. Dong, G. Yuan, Q. Zhang and X. Li, *J. Alloys Compd.*, 2022, **906**, 164302.
30 W. Lai, S. Zhao, M. Guo, D. Wu, S. Luo, C. Zhang, T. Huang, W. He, M. Li and X. Zhou, *et al.*, *Chem. Eng. J.*, 2024, **499**, 156668.
31 Y. Guan, S. Jiang, Y. Ding, B. Xiao, Y. Pi, Z. Wang and Y. Cong, *Mater. Today Energy*, 2024, **44**, 101642.
32 M. Das and S. Ghosh, *J. Phys. D: Appl. Phys.*, 2021, **55**, 085502.
33 P. E. Blöchl, *Phys. Rev. B: Condens. Matter Mater. Phys.*, 1994, **50**, 17953.
34 G. Kresse and D. Joubert, *Phys. Rev. B: Condens. Matter Mater. Phys.*, 1999, **59**, 1758.
35 J. P. Perdew, *Phys. Rev. Lett.*, 1997, **77**, 3868.
36 H. J. Monkhorst and J. D. Pack, *Phys. Rev. B: Condens. Matter Mater. Phys.*, 1976, **13**, 5188.
37 T. Sruthi and K. Tarafder, *Phys. B*, 2021, **604**, 412676.
38 T. Sruthi, N. Devaraj and K. Tarafder, *Electron. Struct.*, 2021, **3**, 025003.
39 L. Wang, J. Wang, Z. Zhang, L. Wang, W. Wang, J. Liu, Z. Hong, K. Cho and W. Wang, *J. Mater. Chem. A*, 2019, **7**, 16231–16238.